

**Time-of-flight modulated intensity small-angle neutron scattering measurement of the self-diffusion constant of water**

Kuhn, Stephen J.; Geerits, Niels; Franz, Christian; Plomp, Jeroen; Dalgliesh, Robert M.; Parnell, Steven R.

**DOI**

[10.1107/S1600576721002612](https://doi.org/10.1107/S1600576721002612)

**Publication date**

2021

**Document Version**

Final published version

**Published in**

Journal of Applied Crystallography

**Citation (APA)**

Kuhn, S. J., Geerits, N., Franz, C., Plomp, J., Dalgliesh, R. M., & Parnell, S. R. (2021). Time-of-flight modulated intensity small-angle neutron scattering measurement of the self-diffusion constant of water. *Journal of Applied Crystallography*, 54, 751-758. <https://doi.org/10.1107/S1600576721002612>

**Important note**

To cite this publication, please use the final published version (if applicable). Please check the document version above.

**Copyright**

Other than for strictly personal use, it is not permitted to download, forward or distribute the text or part of it, without the consent of the author(s) and/or copyright holder(s), unless the work is under an open content license such as Creative Commons.

**Takedown policy**

Please contact us and provide details if you believe this document breaches copyrights. We will remove access to the work immediately and investigate your claim.



# Time-of-flight modulated intensity small-angle neutron scattering measurement of the self-diffusion constant of water

Stephen J. Kuhn,<sup>a,\*‡</sup> Niels Geerits,<sup>b‡</sup> Christian Franz,<sup>c,d</sup> Jeroen Plomp,<sup>e</sup> Robert M. Dalglish<sup>f</sup> and Steven R. Parnell<sup>e</sup>

Received 20 September 2020

Accepted 9 March 2021

Edited by G. J. McIntyre, Australian Nuclear Science and Technology Organisation, Lucas Heights, Australia

‡ Stephen J. Kuhn and Niels Geerits contributed equally to this work.

**Keywords:** water; self-diffusion; neutron scattering; neutron spin echo; modulated intensity small-angle neutron scattering; MI-SANS; water.

<sup>a</sup>Center for Exploration of Energy and Matter, Indiana University, Bloomington, IN 47408, USA, <sup>b</sup>Atominstut, TU Wien, Stadionallee 2, 1020 Vienna, Austria, <sup>c</sup>Physik Department, Technische Universität München, Garching D-85748, Germany, <sup>d</sup>Heinz Maier-Leibnitz Zentrum (MLZ), Technische Universität München, Garching D-85748, Germany, <sup>e</sup>Faculty of Applied Sciences, Delft University of Technology, Mekelweg 15, 2629 JB Delft, The Netherlands, and <sup>f</sup>ISIS, Rutherford Appleton Laboratory, Chilton, Oxfordshire OX11 0QX, UK. \*Correspondence e-mail: stkuhn@iu.edu

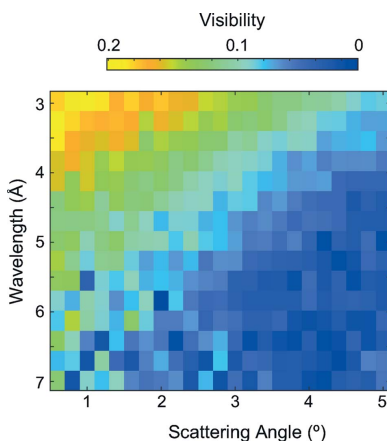
The modulated intensity by zero effort small-angle neutron scattering (MI-SANS) technique is used to measure scattering with a high energy resolution on samples normally ill-suited for neutron resonance spin echo. The self-diffusion constant of water is measured over a  $q$ - $t$  range of  $0.01$ – $0.2 \text{ \AA}^{-1}$  and  $70$ – $500 \text{ ps}$ . In addition to demonstrating the methodology of using time-of-flight MI-SANS instruments to observe diffusion in liquids, the results support previous measurements on water performed with different methods. This polarized neutron technique simultaneously measures the intermediate scattering function for a wide range of time and length scales. Two radio frequency flippers were used in a spin-echo setup with a  $100 \text{ kHz}$  frequency difference in order to create a high-resolution time measurement. The results are compared with self-diffusion measurements made by other techniques and the general applicability of MI-SANS at a pulsed source is assessed.

## 1. Introduction

The dynamics of liquid systems is a complex field where many mechanisms influence the behaviour. In water ( $\text{H}_2\text{O}$ ) and other liquids, short-time-scale dynamics are determined by molecular rotations and vibrations, while long-time-scale dynamics are dominated by self-diffusion. These dynamics are characterized by the intermediate scattering function,  $S(q, \tau)$ . This is a distribution function containing information on the length and time scales of the sample dynamics (Mezei, 2003) such as the self-diffusion constant,  $D$ , which is defined by the stochastic motion of molecules at thermal equilibrium (Price, 2009).

There are several methods for determining the diffusion constant. Molecular dynamics (MD) simulations can compute the intermediate scattering function and diffusion constant, which can be compared with experimental results. Nuclear magnetic resonance (NMR) is an experimental probe of the diffusion constant using gradient echo methods. However, NMR does not give information about the reciprocal-space dependence (Price, 2009). Scattering methods have long been applied to the investigation of water diffusion, and for comprehensive reviews the reader is directed to Price (2009), Amann-Winkel *et al.* (2016) and Holz *et al.* (2000).

In this paper, we present the methodology of using a high-resolution neutron scattering technique to measure the intermediate scattering function and diffusion constant, and apply it to the important case of bulk water at  $\sim 300 \text{ K}$ . The



© 2021 International Union of Crystallography

modulated intensity by zero effort small-angle neutron scattering (MI-SANS, also called MIEZE-SANS) technique is a variant of neutron (resonance) spin echo (Mezei, 1972) (NSE/NRSE) (Golub & Gähler, 1987; Gähler *et al.*, 1992; Hank *et al.*, 1997). Both are very high resolution neutron scattering measurements of dynamics in the picosecond to nanosecond time regime (Franz, Säubert *et al.*, 2019; Lebedev & Torok, 1999; Bleuel *et al.*, 2006, 2009). The basis of MI-SANS is that two radio frequency (RF) flippers are used to create a high-frequency, but resolvable, time oscillation in a neutron intensity signal that is scattered by a sample. MI-SANS is complementary to NRSE and offers several distinct advantages. Most notable for this experiment are that it only requires two RF flippers (as opposed to four in NRSE), leading to an easier instrument setup than traditional NRSE, and that all of the spin manipulations are performed before the sample, so depolarizing samples and sample environments do not impede the measurement. For this experiment on water, the incoherent neutron scattering from hydrogen would reduce the maximum polarization on a conventional NSE instrument to one-third. In MI-SANS, because the polarization does not need to be maintained through the sample, the incoherent scattering simply creates a larger signal at the detector. This is the case for any hydrogenous system, and the insensitivity to depolarization also simplifies the use of sample environments with high magnetic fields.

We have set up the MI-SANS instrument on a time-of-flight beamline with two RF flippers performing  $\pi/2$  flips with a resulting 100 kHz frequency difference, a  $^3\text{He}$  analyser, and a standard  $^3\text{He}$  tube detector array. Time-of-flight MI-SANS measures the intermediate scattering function for a range of scattering angles and wavelengths simultaneously. The instrument was tuned to measure  $S(q, \tau)$  at time scales of  $\sim 50\text{--}500$  ps and scattering vector magnitudes ranging from  $\sim 0.02$  to  $0.07\text{\AA}^{-1}$ , in the domain dominated by self-diffusion for water. We demonstrate the effectiveness of using a time-of-flight MI-SANS instrument for studying liquid dynamics. Additionally, we find a bulk diffusion constant for water of  $2.45 \pm 0.32 \times 10^{-9} \text{ m}^2 \text{ s}^{-1}$ , in good agreement with the NMR literature and which sets a standard for comparison of constrained water samples.

## 2. Methods

The experiment was conducted on the Larmor instrument at the ISIS pulsed neutron and muon source (ISIS DOI 10.5286/ISIS.E.RB1920600). The instrument configuration is shown schematically in Fig. 1. The incident beam polarization is selected to be in the + or - z direction using a polarizer consisting of a v-cavity and a gradient RF flipper (not shown). The neutron precesses in a region with two RF flippers, RF1 and RF2. Before the sample is a spin-polarized  $^3\text{He}$  cell in a

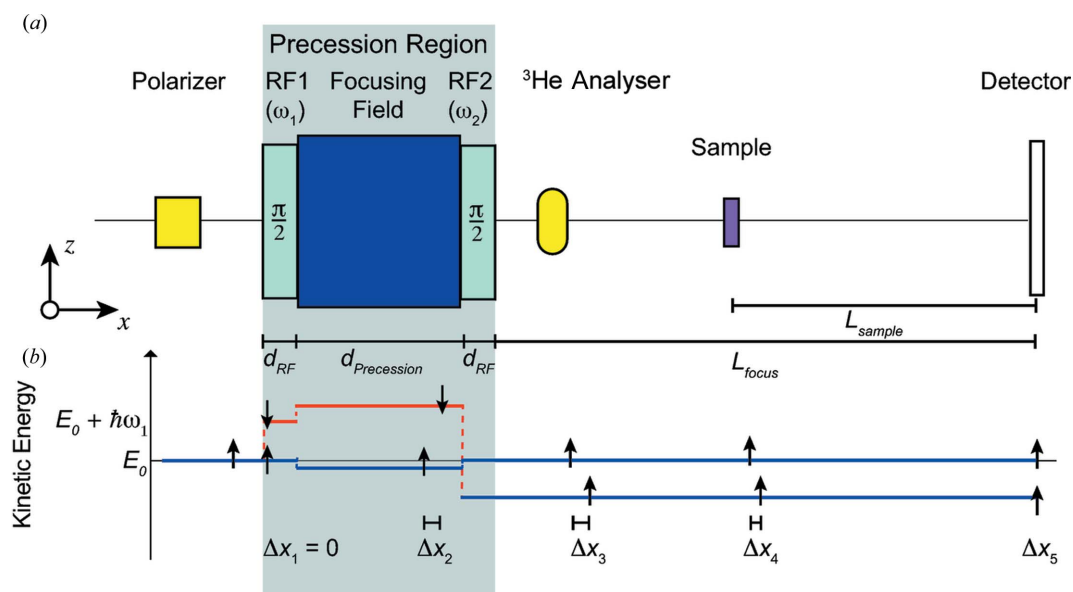


Figure 1

Instrument setup and separation of the neutron states. (a) A side view of the magnetic components of the MI-SANS instrument. The beam travels in the x direction through the polarizer, RF flipper 1 (with angular frequency  $\omega_1$ ), the focusing field (a static z-direction guide field of length  $d_{\text{prec}}$ ) and RF flipper 2 (with frequency  $\omega_2 > \omega_1$ ). Both RF flippers are of length  $d_{\text{RF}}$  and set to perform  $\pi/2$  spin flips, which creates a superposition of up and down spin states. The beam passes through a  $^3\text{He}$  analyser which absorbs the spin down neutron states. The neutron then scatters from the sample and is measured by the two-dimensional detector, which is placed  $L_{\text{focus}}$  away from RF2 and  $L_{\text{sample}}$  away from the sample. (b) The kinetic energy and separation of the spin states are shown along the instrument. The beam is initially polarized in the z direction. The  $\pi/2$  flip in RF1 creates a superposition of the up and down spin states, with the flipped spin state gaining an energy of  $\hbar\omega_1$  from the flipper. In the focusing field, the spin states' kinetic energy is lowered or raised by the Zeeman term. The difference in kinetic energy creates a spatial separation, as shown by  $\Delta x_2$ . RF2 is set to a larger frequency ( $\omega_2$ ) and hence will cause a larger change in energy of the flipped neutron spin. RF2 also creates a superposition of up and down states for the two states entering it, but the  $^3\text{He}$  analyser is set to filter the down state, leaving two different spatially separated ( $\Delta x_3$ ) energy states with the same spin. Because the kinetic energy is different, the spatial separation decreases as the states continue along the beamline. The two energy states pass through the sample with separation  $\Delta x_4$  before reaching the detector with separation  $\Delta x_5$ .

magnetostatic cavity for polarization analysis. The polarizer, flippers and analyser are in a vertical guide field (focusing field) of 8 gauss ( $1 \text{ G} = 10^{-4} \text{ T}$ ) to maintain the neutron polarization. The beam stays within evacuated flight tubes, with the exception of a  $\sim 1 \text{ m}$  region in the sample and  $^3\text{He}$  analyser area. Collimation is achieved with a 15 mm pinhole at the sample position and a  $25 \times 25 \text{ mm}$  aperture located approximately 5 m before the sample position.

The longitudinal RF flippers RF1 and RF2 consist of a vertical ( $\mathbf{z}$  direction) static field and a horizontal RF field. The static field strength is tuned to  $B_{1(2)} = \omega_{1(2)}/\gamma$ , where  $B_{1(2)}$  is the resonance field for RF1 (RF2),  $\omega_{1(2)}$  is the RF frequency and  $\gamma$  is the neutron gyromagnetic ratio. The flippers were separated by 1.57 m and run in  $1/t, \pi/2$  mode, meaning that the RF field strength is ramped to produce a  $\pi/2$  spin flip for each neutron wavelength  $\lambda$ , similar to the setups reported by Zhao *et al.* (2015) and Brandl *et al.* (2012).

The RF flippers in this experiment were tuned to  $\pi/2$  mode in order to simplify the setup of the instrument. In a traditional MI-SANS experiment, the RF flippers perform a  $\pi$  flip, meaning that the initial and final neutron polarization directions must be reoriented with a v-coil (Geerits *et al.*, 2019). In  $\pi/2$  mode, the v-coil is not required, which saves approximately 1 day of setup time but reduces the accessible Fourier time by a factor of two.

Calibration of  $1/t, \pi/2$  mode is performed one flipper at a time. The first step is the tuning of the static field of the flipper, which is accomplished by measuring the beam polarization while scanning the static field in small ( $\sim 0.2 \text{ G}$ ) increments. This field is very sensitive to detuning since the RF coils are quite long. In this step the RF coil is driven using a constant-amplitude sinusoidal waveform (continuous waveform, CW). The beam polarization can be described as a sine function in this mode. At the optimal static field setting the amplitude of this function is maximal. Once the static field is calibrated, the  $1/t$  envelope is calculated using the wavelength at which the first  $\pi$  flip occurs in CW mode and the flipper-to-source separation. Next, the beam polarization is measured with  $1/t$  ramping to confirm all wavelengths are being flipped. Finally, the flipper is switched from  $\pi$  flip mode to  $\pi/2$  mode by halving the current in the RF coil. This current is monitored using a pickup coil which is part of a feedback loop controlling the RF amplifier gain setting. Whether the flipper has been adequately tuned to  $\pi/2$  mode or not can be gauged by measuring the beam polarization, which should be zero for all wavelengths. Once the tuning has been confirmed, the RF coil can be switched off so that the second flipper can be tuned. After tuning both flippers both RF coils can be switched back on to begin  $\pi/2$  MIEZE measurements. In  $\pi/2$  MIEZE the magnetic precession region begins at the first RF flipper, tuned to 533.4 kHz, and ends at the second RF flipper, tuned to 633.4 kHz, producing a frequency difference of 100 kHz.

The MI-SANS focusing condition can be explained as the spatial recombination of two neutron spin states with different group velocities. In the  $\pi/2$  MI-SANS setup, the incoming neutrons are polarized in the  $\mathbf{z}$  direction before entering RF1, which is calibrated to perform a  $\pi/2$  flip of the neutrons. This

yields a superposition of two neutron spin states in the  $\pm z$  directions with different energies. The difference in energies corresponds to a difference in velocities and hence a longitudinal spatial separation between the two spin states. RF2 is set to a higher frequency than RF1, leading to the neutron spin state that was spatially behind having a larger energy (higher velocity) than the spin state that was spatially ahead, as depicted in Fig. 1(b). This difference in energies persists through the  $^3\text{He}$  analyser, which filters spins in the negative  $\mathbf{z}$  direction. Thus, after the analyser, there are two spatially separated neutron states with the same spin direction but different velocities. The relative velocity after the flipper is tuned so that the states will overlap at the desired focal length  $L_{\text{focus}}$  where the detector is placed,

$$L_{\text{focus}} = \frac{\omega_1 d_{\text{prec}} - \int_0^{d_{\text{prec}}} \omega_{\text{FF}}(x) dx}{\Delta\omega} + d_{\text{RF}}. \quad (1)$$

Here,  $d_{\text{RF}}$  is the RF flipper length,  $d_{\text{prec}}$  is the separation between the two RF flippers,  $\omega_1$  is the frequency of the first RF flipper,  $\Delta\omega = \omega_2 - \omega_1$  is the difference in the RF flipper frequencies and  $\omega_{\text{FF}} \simeq \gamma B_{\text{FF}}$ , where  $B_{\text{FF}}$  is the focusing field strength. This term will also include any stray field from the RF flippers (Geerits *et al.*, 2019). When the detector is placed at  $L_{\text{focus}}$ , it will measure an oscillating intensity due to the interference between the energy states (Keller *et al.*, 2002). Thus, the signal can be interpreted as coming from the self-interference of single neutrons. This is shown by the fact that the spin-echo group can be described using the longitudinal autocorrelation of the wavefunction (Golub & Lamoreaux, 1992). Naturally, if the beam contains neutrons described by different wavepackets, the spin-echo group is given by the sum of all possible wavepacket autocorrelations.

In the case of the RF flippers being in  $\pi/2$  mode, the difference frequency is the same as the MI-SANS frequency (Keller *et al.*, 2002; Zhao *et al.*, 2015). In this experiment, the approximately 8 G guide field also served as the focusing field  $B_{\text{FF}}$  between the RF flippers (Jochum *et al.*, 2020). The setup is designed in such a way that the flippers are always situated in a guide field. Hence the range of focusing field values is limited by the constraint that we must not reduce the guide field to a point where the beam depolarizes.

The spatial separation of the neutron spin states is represented in Fig. 1(b) by  $\Delta x$ . At the entrance of RF1 ( $\Delta x_1$ ), the neutron spin states are split into up and down with different kinetic energies, but there is not yet any spatial separation. Before RF2 ( $\Delta x_2$ ), the higher kinetic energy spin state has moved spatially in front of the lower kinetic energy state. Because of the spin flip in RF2, after the  $^3\text{He}$  analyser ( $\Delta x_3$ ), the spin state with the higher kinetic energy is behind the other state. When the states pass through the sample ( $\Delta x_4$ ), they have moved closer together than  $\Delta x_3$ . The focus length  $L_{\text{focus}}$  is tuned so that, if there is no sample in the beam, the states will exactly recombine at the detector as there is no spatial separation ( $\Delta x_5 = 0$ ). The spatial separation can be related to the time separation by  $\Delta t \simeq \Delta x h / (2\lambda E_0)$ , where  $E_0$  is the neutron energy.

$^3\text{He}$  analyser acts as a neutron spin filter to allow through neutrons polarized in the  $z$  direction. The efficiency is wavelength dependent, and characterization of this was performed using transmission measurements (Boag *et al.*, 2007). This gave a  $^3\text{He}$  polarization of 65–70% on each cell change. The  $^3\text{He}$  cell used was a double silicon-window cell with a quartz body, the single-crystal silicon windows being chosen to eliminate the small-angle scattering that occurs with glass cells (Babcock *et al.*, 2013). The cell is 10 cm long along the beam direction, was pressurized to 1 bar (1 bar = 100 000 Pa) and had an on-beam lifetime [exponential decay constant ( $T_1$ )] of  $\sim 100$  hours. The cell was mounted in a magnetostatic cavity similar to the one described by Parnell *et al.* (2009) and monitored using a free induction decay NMR system similar to that described by Parnell *et al.* (2008). The cell was changed each day to maintain a high polarization. The resulting analyser power was  $\sim 90\%$  across the neutron wavelength band used.

The samples were a 1 mm thick cell of deionized water ( $\text{H}_2\text{O}$ ) and a glassy carbon standard (Cappelletti *et al.*, 2018). Measurements alternated between the water and the standard to correct for the time-dependent decay of the  $^3\text{He}$  gas polarization. The water sample was measured at  $\sim 300$  K, which was kept constant by water-bath cooling. The beam size was defined by a 15 mm circular aperture, which gave a detected intensity of 200 neutrons per second. Data were recorded in event mode by a  $60 \times 60$  cm  $^3\text{He}$  tube array with  $0.4 \times 0.8$  cm pixel size, placed 4.45 m from the sample position and 6.45 m from the second RF flipper. Each tube has a thickness of 0.8 cm. The timing resolution of the data acquisition electronics was set to  $1 \mu\text{s}$ , though we note that the effective time resolution also depends on the tube diameter, neutron wavelength and filling pressure. Using Monte Carlo simulations we estimated the expected visibility at various wavelengths. The lower time resolution leads to a simple reduction factor in the visibility, which can be removed through normalization. A discussion of the detector optimization is included below. A beamstop masked the direct beam in order to reduce the background signal, leading to a measurable angle range of  $0.7\text{--}5.5^\circ$ .

### 3. Results

Time-dependent MI-SANS scattering was measured for solid glassy carbon (which acts as a standard) and for water. The glassy carbon data are useful both as a known standard to prove the functionality of MI-SANS and as a way of measuring the instrument resolution function for normalization, since its scattering is purely elastic. The water data can be reduced to obtain the diffusion constant,  $D$ .

MI-SANS characterizes a sample by measuring its visibility. The visibility (also called the contrast) is defined as the intensity difference between the two polarization states divided by their sum:  $V = (I_+ - I_-)/(I_+ + I_-)$ , where  $I_+$  and  $I_-$  are the intensities of the initially up (positive  $z$ ) and down (negative  $z$ ) polarized beams, respectively. MI-SANS measures the visibility for a range of wavelengths and scat-

tering angles. The visibility of the glassy carbon is shown in Fig. 2(a). At large angles the statistics are low due to only the corners of the detector being used. On the detector, the visibility  $V$  is measured with time binning set to  $1 \mu\text{s}$  and an angular binning of  $0.2^\circ$ . This angular binning corresponds to the highest angular resolution with sufficient statistics to obtain good fits. Each pixel within Fig. 2(a) contains 2000 of these time bins. The visibility of each pixel is determined by fitting the amplitude of the time-oscillating polarization signal to a cosine function.

Fig. 2(b) shows a subset of the pixel at  $0.9\text{--}1.1^\circ$  and  $4.3\text{--}4.5 \text{ \AA}$ , and the cosine fit used to determine the visibility. The wavelength corresponds directly to the detector time. For clarity, only a portion of the time bins in the pixel are shown. The visibility of the glassy carbon is not corrected for the  $^3\text{He}$  analyser transmission and background counts were found to be negligible compared with the signal.

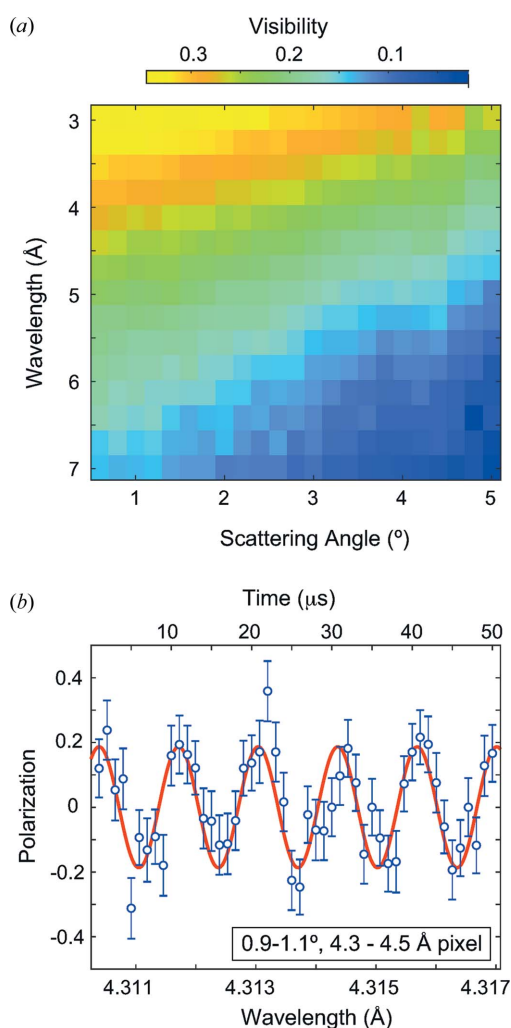


**Figure 2** (a) The visibility of glassy carbon versus angle and wavelength. (b) The polarization versus wavelength for part of a single pixel of scattering angle  $0.9\text{--}1.1^\circ$ . On the Larmor time-of-flight instrument, wavelength corresponds to the detector measurement time (top x axis). Error bars represent the statistical counting error. The modulation is fitted using a cosine function (red curve) to find the visibility. The period is  $10 \mu\text{s}$ , as expected from the 100 kHz MI-SANS frequency.

The glassy carbon scattering does not contain any dynamics. Furthermore, the background-to-signal ratio is sufficiently small that the background can be ignored. Therefore, the visibility is fully determined by the reduction factor and instrument limitations (Martin, 2018). However, self-diffusion of the water sample causes a Fourier time-dependent shift to the scattering, as the scattering amplitude is dependent on the energy transfer between the sample and the beam. This is an inherent characteristic of water that we measure with MI-SANS.

The visibility of the MI-SANS signal from water (Fig. 3) is determined by the same procedure as is used for the glassy carbon, except the data are background subtracted to account for a higher relative background rate. The background is corrected by including an extra term in the visibility definition,  $V_{\text{BG}} = (I_+ - I_-)/(I_+ + I_- + 2I_{\text{BG}})$ . This assumes the background is from air and other parasitic scattering along the beamline, leading to an unpolarized background that is the same for  $I_+$  and  $I_-$  and thus cancels on the numerator.

A correction matrix,  $\alpha$ , is defined for the background at each pixel,

$$V_{\text{BG}} = \frac{I_+ - I_-}{(I_+ + I_-)[1 + \alpha]} = \frac{V}{1 + \alpha}. \quad (2)$$

The correction matrix  $\alpha$  is found using the background data taken with the sample removed from the beam. The  $I_+$  and  $I_-$  background data are binned in the same manner as the water data. Because only the sum of  $I_+$  and  $I_-$  is needed, all 2000 time bins are summed to increase statistics. To determine the background-corrected visibility, each visibility pixel is multiplied by the corresponding  $1 + \alpha$  value.

The MI-SANS results can be directly converted into the more conventional neutron scattering parameters of scattering vector magnitude  $q$  and time  $\tau$ . In the case of elastic scattering where the energy transfer is negligible, the  $q$  value is deter-

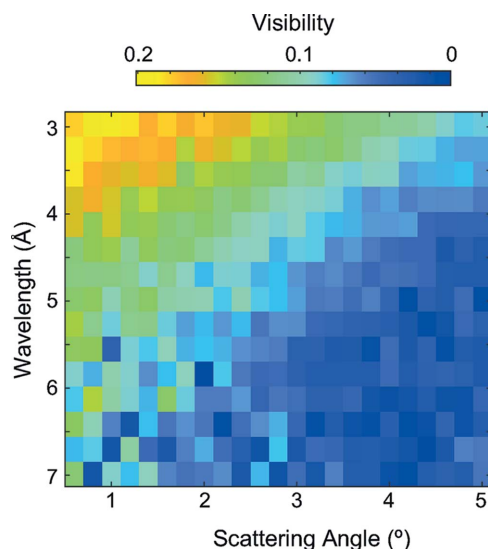


**Figure 3**  
The visibility of water versus angle and wavelength. For each pixel, the modulation amplitude is fitted by a cosine function to get the visibility, after correcting for the  $^3\text{He}$  analyser efficiency and air scattering background using equation (2).

mined by the scattering angle and the wavelength:  $q_e = 4\pi \sin(\theta/2)/\lambda$ . For quasi-elastic scattering a first-order correction must be applied,  $q_{qe} = q_e + \Delta q$ , which takes the energy transfer into account. It can be shown that  $\Delta q = \pm(m\omega/\hbar k) \sin(\theta/2)$ , with  $\hbar\omega$  the scattering energy and  $k$  the initial wavevector. In this experiment the first-order correction amounts to only 1–2% at most and is therefore neglected, and  $q$  is assumed to be radially isotropic. At small scattering angles,  $\sin(\theta/2) \simeq \theta/2$  and several points are at equivalent  $q$  in Figs. 2(a) and 3. The Fourier time  $\tau$  is defined as the neutron phase shift over the angular frequency  $\tau = \Delta\phi/\Omega$ , with  $\Omega$  the neutron angular frequency. The phase shift can also be written in terms of the instrument parameters  $\Delta\phi = \Delta\omega t$ , where  $t$  is the time the neutron takes to travel between the sample and the detector. The Fourier time can be written in terms of  $L_{\text{sample}}$ ,

$$\tau = \frac{\Delta\omega m_n^2 \lambda^3}{2\pi \hbar^2} L_{\text{sample}}, \quad (3)$$

where  $m_n$  is the neutron mass (Franz, Säubert *et al.*, 2019; Keller *et al.*, 2002).

The ratio of the visibilities of the water sample and the glassy carbon sample yields the intermediate scattering function  $S(q, \tau) = [V_{\text{water}}(q, \tau)]/[V_{\text{carbon}}(q, \tau)]$  of water. In this  $\tau$ - $q$  domain the dynamics in water are dominated by self-diffusion, while other inelastic processes such as vibration and rotation of the molecules can be ignored. The position of a water molecule can therefore be modelled using the diffusion equation

$$\frac{\partial}{\partial \tau} G(r, r', \tau) = D \nabla^2 G(r, r', \tau) \\ G(r, r', 0) = \delta(r - r') \quad \lim_{\tau \rightarrow \infty} G(r, r', \tau) = 0, \quad (4)$$

where  $D$  is the self-diffusion coefficient and  $G(r, r', \tau)$  is the van Hove correlation function, describing the probability of finding a water molecule at position  $r$  and time  $\tau$ . We assume that at  $\tau = 0$  the position of the molecule is well defined at  $r = r'$ . The solution is simply a Gaussian function,

$$G(r, r', \tau) = \frac{1}{(4\pi D\tau)^{1/2}} \exp\left[-\frac{(r - r')^2}{4D\tau}\right]. \quad (5)$$

This function models the probability density of finding a water molecule at position  $r$  and time  $\tau$ , given that at  $\tau = 0$  the particle was located at  $r = r'$ . To determine the intermediate scattering function we must calculate the Fourier transform of  $G(r, r', \tau)$  with respect to  $r$ ,

$$S(q, r', \tau) = c \int G(r, r', \tau) \exp(-iqr) dr \\ = a \exp(-iqr') \exp(-Dq^2\tau). \quad (6)$$

The amplitude factor  $a$  models the fast dynamics at low  $\tau$ , which are not taken into account by diffusion. The visibility can be obtained by averaging in  $r'$  over the sample volume  $D$ ,

$$V = RS_D(q, \tau) = aR \exp(-Dq^2\tau) \int_D \exp(-iqr') dr', \quad (7)$$

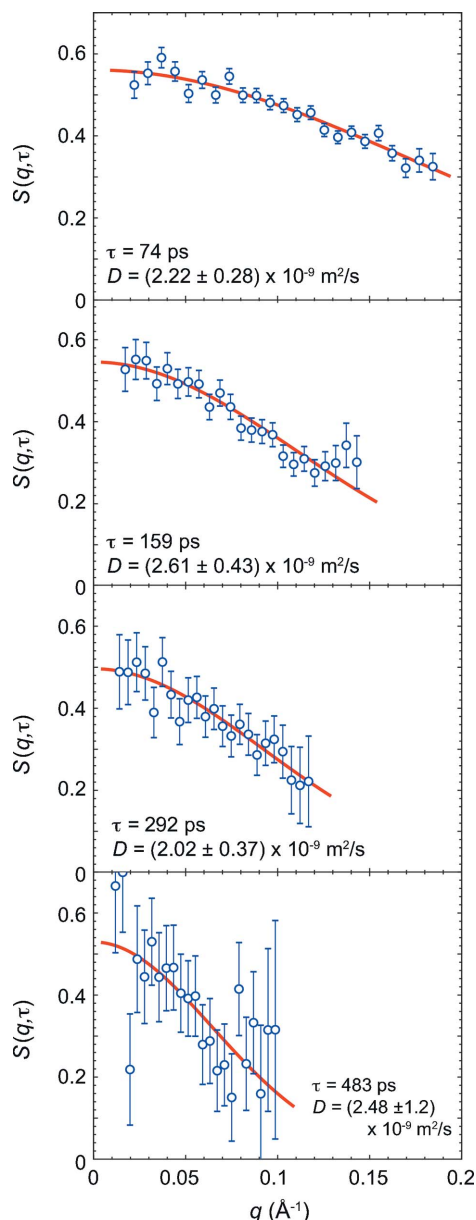


**Figure 4**  
 $S(q, \tau)$  values plotted at four Fourier times  $\tau$ . Each  $\tau$  corresponds to a specific wavelength of 2.95, 3.85, 4.65 and 5.55  $\text{\AA}$ , respectively, with 0.3  $\text{\AA}$  bins. Error bars correspond to the MI-SANS visibility fit uncertainty from each pixel. The diffusion constant  $D$  is fitted from  $S(q, \tau)$  using equation (8).

with  $R$  a reduction factor due to various factors pertaining to instrument resolution (e.g. timing resolution). To remove contributions from the instrument resolution we normalize  $S_D(q, \tau)$  by the intermediate scattering function of a static sample (in this case, the glassy carbon). Ideally, the position of the atoms in this sample can be described by  $G(r, r', \tau) = \delta(r - r')$ . The Fourier transform  $\exp(-iqr)$  yields the visibility for this ideal sample:  $V_0 = \int_D \exp(-iqr') dr'$ . The intermediate scattering function can therefore be derived as

$$S(q, \tau) = \frac{V(q, \tau)}{V_0(q, \tau)} = a \exp(-Dq^2\tau). \quad (8)$$

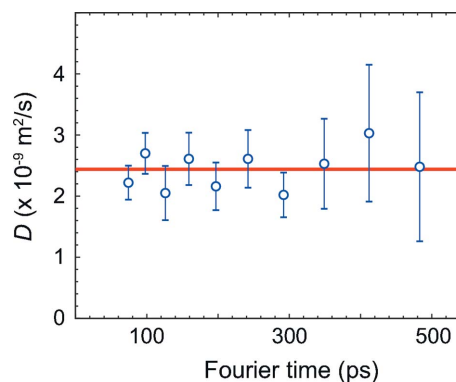


**Figure 5**  
 Diffusion constants for water extracted from the fit of  $S(q, \tau)$  for each Fourier time  $\tau$ . The average value of  $2.4 \times 10^{-9} \text{ m}^2 \text{ s}^{-1}$  is shown by the red line. Error bars correspond to the 70% confidence region of the fit.

In this MI-SANS experiment, the intermediate scattering function is given by the ratio between the water and glassy carbon visibilities.  $S(q, \tau)$  is plotted for several Fourier times in Fig. 4. Each Fourier time is effectively a normalized horizontal slice in the visibility plot (Fig. 3). However, the  $q$  range measured for each  $\tau$  is different, with higher  $\tau$  having a smaller range. The data at each  $\tau$  are fitted using equation (8).

The diffusion constants extracted for each Fourier time are shown in Fig. 5. The average value, shown by the red line, is  $2.45 \pm 0.32 \times 10^{-9} \text{ m}^2 \text{ s}^{-1}$ , which is within the error bars for each Fourier time, so no trend is seen.

#### 4. Discussion

Our results expand upon previous measurements of the dynamics of water at ambient temperature obtained by neutron scattering and NMR. Previous quasi-elastic neutron scattering (QENS) measurements considering water diffusion used a random-jump diffusion model, which applies well to the small  $q$  values used in this experiment, but also to larger  $q$  (Teixeira *et al.*, 1985; Cavatorta *et al.*, 1994; Egelstaff *et al.*, 1967). A diffusion constant of  $2.36 \times 10^{-9} \text{ m}^2 \text{ s}^{-1}$  was found (Cavatorta *et al.*, 1994).

NMR is frequently used to measure diffusion in liquids and several measurements have been made on water. There are a wide range of diffusion constant values that can be measured with NMR. NMR relaxometry is useful for slower materials ( $D$  down to  $10^{-9} \text{ m}^2 \text{ s}^{-1}$ ) (Kruk *et al.*, 2012) and NMR pulsed-gradient field methods are useful for the range of  $10^{-6}$ – $10^{-14} \text{ m}^2 \text{ s}^{-1}$  (Price, 2009). NMR results for water at  $\sim 300$  K have generally shown values around  $2.3 \times 10^{-9} \text{ m}^2 \text{ s}^{-1}$ , within the error bars of the MI-SANS results (Trappeniers *et al.*, 1965; Wiengärtner, 1982). One difference between MI-SANS and NMR is that MI-SANS does not need to apply a magnetic field to the samples, so samples that induce stray fields can be studied without extra corrections.

Another purpose of this experiment was to compare our MI-SANS measurement on a pulsed source with measurements performed at a continuous source. The implementation of MI-SANS geometry has been proposed on a pulsed source (Bleuel *et al.*, 2005, 2006) and demonstrated using a reactor

source with a chopper on a skyrmion system (Brandl *et al.*, 2012). The RESEDA beamline at the FRM-II neutron source (at the MLZ, Munich, Germany) has performed many MI-SANS experiments at constant wavelength (Franz, Säubert *et al.*, 2019; Franz, Soltwedel *et al.*, 2019). The direct advantages of a continuous source are an easier determination of the  $q$  value at various points on the detector and, usually, an overall higher neutron flux. However, a pulsed source can use the modulation in the wavelength spread as a way of tuning the length  $L_{\text{focus}}$  (Geerits *et al.*, 2019). Additionally, the detector simultaneously measures a wide range of Fourier times and  $q$  ranges, leading to an efficient use of the different neutron wavelengths. We measured  $q$  scans for ten Fourier times, despite the relatively low scattering from the water sample. This also means that the MI-SANS time can be changed without retuning the RF flippers. A pulsed source still offers some flexibility in terms of acquiring sufficient statistics because the wavelength/time bins can be rescaled to include more modulations, leading to a lower error in the fit (in our case, each bin included 2000 points), although ultimately a continuous source will have the maximum flexibility of choosing each Fourier time measured.

The MI-SANS technique can be applied to many other materials to measure the intermediate scattering function and self-diffusion. Materials with diffusion ten times slower or 100 times faster than water could both be fitted with MI-SANS on the Larmor instrument, as shown by the expected curves for those materials in Fig. 6. The listed Fourier times can be achieved by adjusting  $\Delta\omega$  within its tolerance on Larmor. The  $q$  range could be expanded even more by adjusting the detector position in the  $y$  direction and, with careful setup, the  $\Delta\omega$  could be even larger. MI-SANS is especially useful in hydrogenous materials, where conventional neutron spin echo has limited polarization (Franz, Säubert *et al.*, 2019). Another useful feature is that it can accept a wide variety of sample environments, including strong magnetic fields (Kindervater *et al.*, 2015). One application we foresee is measuring the diffusion of liquid neutron moderators. Their design depends on a good understanding of their diffusion and they are often hydrogenous (Iverson *et al.*, 2018).

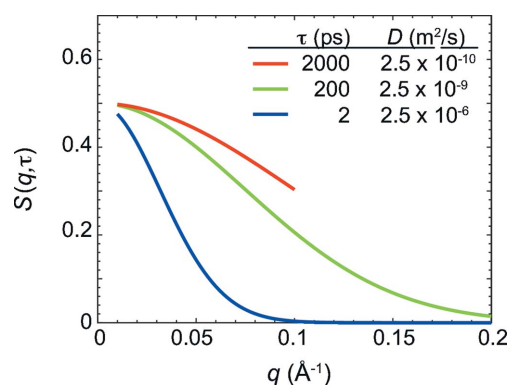


**Figure 6**  
The range of diffusion constants that can be measured with the MI-SANS technique on the Larmor instrument. The lines represent the maximum (blue), minimum (red) and water (green) intermediate scattering functions on the Larmor instrument set to the appropriate Fourier time  $\tau$ .

As well as selecting a pulsed or continuous source, there are also multiple options in choosing what type of neutron analyser to use. In this experiment a  $^3\text{He}$  analyser was used instead of a supermirror. The  $^3\text{He}$  cell has less background scattering at low  $q$  than a supermirror but reduces the overall polarization. Additionally, the  $^3\text{He}$  cell's neutron transmission varies significantly across neutron wavelengths and the cell must be repolarized several times throughout an average experiment.

We have implemented this technique on an existing polarized SANS instrument using the coils that were developed for Larmor labelling (Geerits *et al.*, 2019), and despite the good agreement of the diffusion constant with other measurements, several areas for improvement remain. First, the detector causes a significant loss in the intensity modulation signal, as the tubes are 0.8 cm diameter. This reduces the effective timing resolution of the detector as the neutron velocity decreases. Using measurements of detector transmission and Monte Carlo modelling of neutron absorption in the detector, we calculated a maximum visibility of 54% at 3 Å, dropping to ~20% at 5 Å. This visibility reduction is solely caused by the detector. Visibility can be improved by utilizing a Cascade detector with a gas electron multiplier (GEM) with a much thinner active area (Köhli *et al.*, 2016). Improvements to the  $^3\text{He}$  polarization of 60–70% in our setup are also possible, with 88+% now being achieved (Chen *et al.*, 2014). It is also possible to remove the time dependence by online pumping (Boag *et al.*, 2009; Parnell *et al.*, 2015; Salhi *et al.*, 2019). Further gains in flux at the sample position are possible by utilizing guides before the sample, although this is a compromise between flux and  $q$  range as this will transport more neutron divergence.

## 5. Conclusion

We have shown that the MI-SANS technique can be simply applied to measure the intermediate scattering function and self-diffusion constant across a wide range of Fourier time scales. Applying this technique to water, we measured the intermediate scattering function from  $q = 0.01 \text{ \AA}^{-1}$  to  $q = 0.18 \text{ \AA}^{-1}$  and at Fourier times from 74 to 570 ps. Fitting the data to equation (8) yielded diffusion constants with an average value of  $2.45 \pm 0.32 \times 10^{-9} \text{ m}^2 \text{ s}^{-1}$ , an intermediate point compared with other values reported in the literature.

Like other neutron techniques, there are distinct differences between its application at a continuous source and a time-of-flight source. The ease of tuning the MI-SANS frequency, the simultaneous collection across many MI-SANS times and the ability to rebin data in the analysis are all distinct advantages of using a pulsed source. We envision the time-of-flight MI-SANS technique that we have described here being used on liquids in many sample environments.

## Acknowledgements

We acknowledge useful discussions with Ad van Well, Dave Baxter and Roger Pynn. We acknowledge the support of Mark

Davenport and Emily McFarlane for the  $^3\text{He}$  cell polarization and installation.

## Funding information

This work was partially financed by the Austrian Science Fund (FWF), project Nos. P30677 and P34239. Part of this research was funded by NWO groot (grant No. LARMOR 721.012.102). SJK was supported by US Department of Commerce cooperative agreement No. 70NANB15H259 and by the US Department of Energy STTR program through grant DE-SC0017127.

## References

- Amann-Winkel, K., Bellissent-Funel, M., Bove, L. E., Loerting, T., Nilsson, A., Paciaroni, A., Schlesinger, D. & Skinner, L. (2016). *Chem. Rev.* **116**, 7570–7589.
- Babcock, E., Salhi, Z. & Ioffe, A. (2013). *J. Phys. Soc. Jpn.*, **82**, SA030.
- Bleuel, M., Bröll, M., Lang, E., Littrell, K., Gähler, R. & Lal, J. (2006). *Physica B*, **371**, 297–301.
- Bleuel, M., Gähler, R., Lang, E. & Lal, J. (2009). *Nucl. Instrum. Methods Phys. Res. A*, **600**, 220–222.
- Bleuel, M., Littrell, K., Gähler, R. & Lal, J. (2005). *Physica B*, **356**, 213–217.
- Boag, S., Babcock, E., Andersen, K. H., Becker, M., Charlton, T. R., Chen, W. C., Dalgliesh, R. M., Elmore, S. D., Frost, C. D., Gentile, T. R., Lopez Anton, R., Parnell, S. R., Petoukhov, A. K., Skoda, M. W. A. & Soldner, T. (2009). *Physica B*, **404**, 2659–2662.
- Boag, S., Parnell, S. R., Frost, C. D., Andersen, K. H. & Babcock, E. (2007). *Physica B*, **397**, 179–181.
- Brandl, G., Lal, J., Carpenter, J., Crow, L., Robertson, L., Georgii, R., Böni, P. & Bleuel, M. (2012). *Nucl. Instrum. Methods Phys. Res. A*, **667**, 1–4.
- Cappelletti, R. L., Udovic, T. J., Li, H. & Paul, R. L. (2018). *J. Appl. Cryst.* **51**, 1323–1328.
- Cavatorta, F., Deriu, A., Cola, D. D. & Middendorf, H. D. (1994). *J. Phys. Condens. Matter*, **6**, A113–A117.
- Chen, W. C., Gentile, T. R., Ye, Q., Walker, T. G. & Babcock, E. (2014). *J. Appl. Phys.* **116**, 014903.
- Egelstaff, P. A., Haywood, B. C. & Webb, F. J. (1967). *Proc. Phys. Soc.* **90**, 681–696.
- Franz, C., Säubert, S., Wendl, A., Haslbeck, F. X., Soltwedel, O., Jochum, J. K., Spitz, L., Kindervater, J., Bauer, A., Böni, P. & Pfeiderer, C. (2019). *J. Phys. Soc. Jpn.*, **88**, 081002.
- Franz, C., Soltwedel, O., Fuchs, C., Säubert, S., Haslbeck, F., Wendl, A., Jochum, J. K., Böni, P. & Pfeiderer, C. (2019). *Nucl. Instrum. Methods Phys. Res. A*, **939**, 22–29.
- Gähler, R., Golub, R. & Keller, T. (1992). *Physica B*, **180–181**, 899–902.
- Geerits, N., Parnell, S. R., Thijs, M. A., van Well, A. A., Franz, C., Washington, A. L., Raspino, D., Dalgliesh, R. M. & Plomp, J. (2019). *Rev. Sci. Instrum.* **90**, 125101.
- Golub, R. & Gähler, R. (1987). *Phys. Lett. A*, **123**, 43–48.
- Golub, R. & Lamoreaux, S. K. (1992). *Phys. Lett. A*, **162**, 122–128.
- Hank, P., Besenböck, W., Gähler, R. & Köppe, M. (1997). *Physica B*, **234–236**, 1130–1132.
- Holz, M., Heil, S. R. & Sacco, A. (2000). *Phys. Chem. Chem. Phys.* **2**, 4740–4742.
- Iverson, E. B., Baxter, D. V., Gallmeier, F. X., Gillis, R. C., Hügle, T., Lu, W., McClanahan, T. C., Remec, I. & Rinckel, T. C. (2018). *J. Phys. Conf. Ser.* **1021**, 012067.
- Jochum, J. K., Wendl, A., Keller, T. & Franz, C. (2020). *Meas. Sci. Technol.* **31**, 035902.
- Keller, T., Golub, R. & Gähler, R. (2002). *Scattering*, edited by R. Pike & P. Sabatier, pp. 1264–1286. London: Academic Press.
- Kindervater, J., Martin, N., Häußler, W., Krautloher, M., Fuchs, C., Mühlbauer, S., Lim, J. A., Blackburn, E., Böni, P. & Pfeiderer, C. (2015). *EPJ Web Conf.* **83**, 03008.
- Köhli, M., Klein, M., Allmendinger, F., Perrevoort, A.-K. T., Schröder, T., Martin, N., Schmidt, C. J. & Schmidt, U. (2016). *J. Phys. Condens. Matter*, **746**, 012003.
- Kruk, D., Meier, R. & Rössler, E. A. (2012). *Phys. Rev. E*, **85**, 020201.
- Lebedev, V. T. & Torok, D. (1999). *Tech. Phys. Lett.* **25**, 116–118.
- Martin, N. (2018). *Nucl. Instrum. Methods Phys. Res. A*, **882**, 11–16.
- Mezei, F. (1972). *Z. Phys.* **1972**, 146–160.
- Mezei, F. (2003). *Neutron Spin Echo Spectroscopy: Basics, Trends and Applications*, ch. 15–31, pp. 5–14. Berlin, Heidelberg: Springer.
- Parnell, S. R., Babcock, E., Nünighoff, K., Skoda, M. W. A., Boag, S., Masalovich, S., Chen, W. C., Georgii, R., Wild, J. M. & Frost, C. D. (2009). *Nucl. Instrum. Methods Phys. Res. A*, **598**, 774–778.
- Parnell, S. R., Washington, A. L., Li, K., Yan, H., Stonaha, P., Li, F., Wang, T., Walsh, A., Chen, W. C., Parnell, A. J., Fairclough, J. P. A., Baxter, D. V., Snow, W. M. & Pynn, R. (2015). *Rev. Sci. Instrum.* **86**, 023902.
- Parnell, S. R., Woolley, E. B., Boag, S. & Frost, C. D. (2008). *Meas. Sci. Technol.* **19**, 045601.
- Price, W. S. (2009). *NMR Studies of Translational Motion*. Cambridge University Press.
- Salhi, Z., Babcock, E., Bingöl, K., Bussmann, K., Kammerling, H., Ossovy, V., Heynen, A., Deng, H., Hutanu, V., Masalovich, S., Voigt, J. & Ioffe, A. (2019). *J. Phys. Conf. Ser.* **1316**, 012009.
- Teixeira, J., Bellissent-Funel, M.-C., Chen, S. H. & Dianoux, A. J. (1985). *Phys. Rev. A*, **31**, 1913–1917.
- Trappeniers, N. J., Gerritsma, C. J. & Oosting, P. H. (1965). *Phys. Lett.* **18**, 256–257.
- Wiengärtner, H. (1982). *Z. Phys. Chem.* **132**, 129–149.
- Zhao, J., Hamilton, W. A., Lee, S. W., Robertson, J. L., Crow, L. & Kang, Y. W. (2015). *Appl. Phys. Lett.* **107**, 113508.